# Structural mechanism of co-import of H2A-H2B and its chaperone Nap1 by nuclear import receptor Kap114

Jenny Jiou[1], Ho Yee Joyce Fung[1] and Yuh Min Chook[2]

Department of Pharmacology, University of Texas Southwestern Medical Center, Dallas, TX 75390, USA.

[1]Authors contributed equally to this work.

[2]Correspondence: yuhmin.chook@utsouthwestern.edu

**Author Contributions:** Conceptualization, Y.M.C.; Methodology and data validation, Y.M.C., J.J., H.Y.J.F.; Investigation, J.J., H.Y.J.F.; Writing, Y.M.C, H.Y.J.F

**Competing Interest Statement:** No competing interest declared.

**Classification:** Biological Sciences: Biophysics and Computational Biology

**Keywords:** Karyopherin, Histones, Chaperone, Importin, Nucleosome

**This PDF file includes:**

Main Text

Table 1

Figures 1 to 4

**Abstract**

Histones are synthesized and processed in the cytoplasm and then transported into the nucleus for assembly into nucleosomes. H2A-H2B is imported into the *S. cerevisiae* nucleus by the importin Kap114, which also imports the most prominent H2A-H2B chaperone, Nap1. We understand how Kap114 recognizes H2A-H2B for nuclear import, but little is known about how it recognizes Nap1. Furthermore, the ternary complex of Nap1, H2A-H2B and Kap114 was previously detected in both the cytosol and the nucleus, but its role in nuclear import is unclear. Here, we present biophysical analysis of interactions between Nap1, H2A-H2B, Kap114 and RanGTP, and cryo-electron microscopy structures of ternary Kap114, Nap1 and H2A-H2B complexes. Kap114 binds Nap1 very weakly, but H2A-H2B enhances Kap114-Nap1 interaction to form a ternary Kap114/Nap1/H2A-H2B complex that is stable in the absence and presence of RanGTP. Cryogenic electron microscopy structures reveal two distinct ternary Kap114/Nap1/H2A-H2B complexes: a 3.2 Å resolution structure of Nap1 bound to H2A-H2B-bound Kap114 where Nap1 does not contact H2A-H2B, and a 3.5 Å resolution structure of H2A-H2B sandwiched between Nap1 and Kap114. Collectively, these results lead to a mechanistic model of how Nap1•H2A-H2B encounters Kap114 in the cytoplasm and how both H2A-H2B and Nap1 are chaperoned and co-imported by Kap114 into the nucleus. The model also suggests how RanGTP-binding stabilizes a quaternary RanGTP/Kap114/Nap1/H2A-H2B complex that facilitates hand-off of H2A-H2B from Kap114 to Nap1, the assembling nucleosome or other nuclear chaperone.

## Significance Statement

Free core histones are highly toxic and must be sequestered by other macromolecules in the cell. The mechanism of H3-H4 import by karyopherin Importin-4 in the presence of its chaperone ASF1 is understood, but the mechanism of how histone chaperone Nap1 influences H2A-H2B import is not resolved. We present biophysical interaction analysis and cryo-EM structures that reveal how Kap114, Nap1 and H2A-H2B assemble into an import complex. These results lead us to a structural mechanism of how Nap1 delivers H2A-H2B to Kap114 in the cytosol, how Nap1 and H2A-H2B are co-imported into the nucleus, and how RanGTP may influence Kap114/Nap1/H2A-H2B interactions to assemble nucleosomes in the nucleus.

## Introduction

Formation of new nucleosomes to pack newly replicated DNA during the S-phase of the cell cycle begins with rapid synthesis of core histones H3, H4, H2A and H2B followed by their rapid transport into the nucleus. As H3 and H4 emerge from translating ribosomes, they are folded into H3-H4 heterodimers by heat shock proteins and histone chaperones, acetylated at several lysine side chains (1-3) and then passed to histone chaperone ASF1 and *H. sapiens* (*Hs*) nuclear import receptor (also termed importin) Importin-4 or its *S. cerevisiae* (*Sc*) homolog Kap123 for transport across the nuclear pore complex (NPC) into the nucleus (4-7). The steps of H2A-H2B biosynthesis and processing in the cytoplasm have not been delineated, but selective ribosome profiling to measure nascent chain association of all *Sc* importins showed no importin association

with the nascent chains of H2A and H2B (8). Thus, H2A-H2B likely follow a similar path as H3-H4 that involves a network of heat shock proteins to fold them into H2A-H2B dimers, histone chaperones to prevent aberrant and toxic interactions of the highly aggregation-prone histones, and an importin for transport across the NPC.

The heat shock proteins/folding chaperones for H2A and H2B have not been identified, but it is well-established that H2A-H2B binds to a histone chaperone named Nucleosome Assembly Protein 1 (Nap1) in the *Sc* cytoplasm and several homologous Nap1 chaperones in *Hs* cells (9-13). The importin primarily responsible for H2A-H2B nuclear import is also known - *Sc* Karyopherin-114 (Kap114) and its *Hs* homolog Importin-9 (IMP9 or IPO9) in *Hs* and *Sc* cells, respectively. *Sc* Kap123 and Kap121 and their *Hs* homologs Importin-4 (IMP4 or IPO4) and Importin-5 (IMP5 or IPO5) are secondary or backup importins for nuclear import of H2A-H2B (14). Interestingly, Kap114 also binds and transports *Sc* Nap1 into the nucleus, and histones appear to increase the association of Nap1 with Kap114 in a pull-down assay (9, 15). Thus, Kap114, H2A-H2B and Nap1 proteins likely associate into one assembly in the cytoplasm and translocate together across the NPC into the nucleus. Interactions between them seemed to persist in the presence of RanGTP and the complex containing Kap114, Nap1 and H2A-H2B was detected in *Sc* nuclear extract, suggesting that both Nap1 and Kap114 continue to chaperone H2A-H2B even after entry into the nucleus (15).

Histone proteins H2A and H2B contain disordered N- and C-terminal tails as well as central regions that fold together into the globular H2A-H2B histone-fold domain (Figure 1A) (16). The symmetric *Sc* Nap1 homodimer binds the histone-fold of H2A-H2B and shield its DNA-binding regions (17, 18). The 114 kDa Kap114 contains 20 HEAT

repeats (h1-h20, each composed of a pair of anti-parallel helices a and b) that are organized into a superhelix (Figure 1A) (19). The superhelical Kap114 wraps its N- and C-terminal HEAT repeats around the H2A-H2B histone-fold domain and also shields the histone's DNA- and H3-H4-binding regions (20).

We understand how Kap114 binds H2A-H2B and how Nap1 binds H2A-H2B, but we do not know how Kap114 binds Nap1, and how H2A-H2B increases the interaction between Kap114 and Nap1 to form a nuclear import complex. Furthermore, once in the nucleus, this import complex will bind RanGTP, and H2A-H2B will need to be released to either a nuclear chaperone or to the assembling nucleosome. The structure of Kap114 bound to both H2A-H2B and RanGTP was recently reported, revealing how RanGTP binding to Kap114 modifies the Kap114-H2A-H2B interactions within the RanGTP•Kap114•H2A-H2B ternary complex to facilitate its transfer to the assembling nucleosome or to other nuclear chaperones (20). It is not known how Nap1 affects the structure and function of this RanGTP•Kap114•H2A-H2B complex.

Here we reveal the structural mechanism of H2A-H2B and Nap1 co-import into the nucleus by Kap114 through biophysical analysis and cryogenic electron microscopy (cryo-EM) structures of different complexes that contain Nap1, Kap114 and H2A-H2B. We also present biophysical analysis of interactions between Kap114, Nap1 and H2A-H2B in the presence of RanGTP that lead to a model for how they interact in the nucleus and how RanGTP modulates those interactions in the nucleus.

## Results and Discussion

### Kap114 binds a Nap1 dimer

The 48 kDa Nap1 contains a disordered N-terminal tail (residues 1-73), a core domain (74-365, 34 kDa) that dimerizes or oligomerizes and an acidic C-terminal tail (residues 366-417) (Figure 1A). Pemberton and colleagues reported that Kap114 binds residues in the Nap1 core domain (15). We measured the affinity of Kap114 for the Nap1 core (residues 74-365) by analytical ultracentrifugation (AUC), which showed a weak dissociation constant ($K_D$) of 1 [0.5, 2.7] μM (95% confidence interval in brackets) (Figure 1B and Figure S1A). Analysis of the estimated molecular weight for the Kap114•Nap1 complex (178 kDa) suggested a stoichiometry of one Kap114 molecule binding to a Nap1 dimer (theoretical molecular weight of 186 kDa) (Figure 1B). We also performed size exclusion chromatography multi-angle light scattering (SEC-MALS) analysis with the full length (FL) Nap1 protein. Nap1 FL is a tetramer with an apparent molecular mass of ~200 kDa (Figure S1B). Analysis of a mixture of 1:1 molar ratio of Kap114:Nap1 dimer resulted in a peak of ~ 220 kDa that matches the mass of a complex of one Kap114 molecule binding to one Nap1 dimer; the Kap114•Nap1 complex has a similar elution volume as the Nap1 tetramer but has a higher differential refractive index (DRI) that is consistent with the incorporation of Kap114 (Figure S1B). Altogether, biophysical analyses show one Kap114 binding weakly to one Nap1 dimer.

**A ternary complex of Kap114 binding to a H2A-H2B heterodimer and a Nap1 dimer**

We probed interactions between Kap114 and the Nap1 core in the presence and absence of *X. laevis (Xl)* H2A-H2B by pull-down binding assays using immobilized MBP-Kap114. Kap114 pulled down more Nap1 core when H2A-H2B is present (Figure 1C). This result is consistent with previous results of pull-down assays using immobilized GST-

Nap1 FL with MBP-Kap114 and chicken histones (15). The more quantitative fluorescent polarization (FP) analysis using $^{XFD488}$Nap1 FL (XFD488 is conjugated to C414 in the

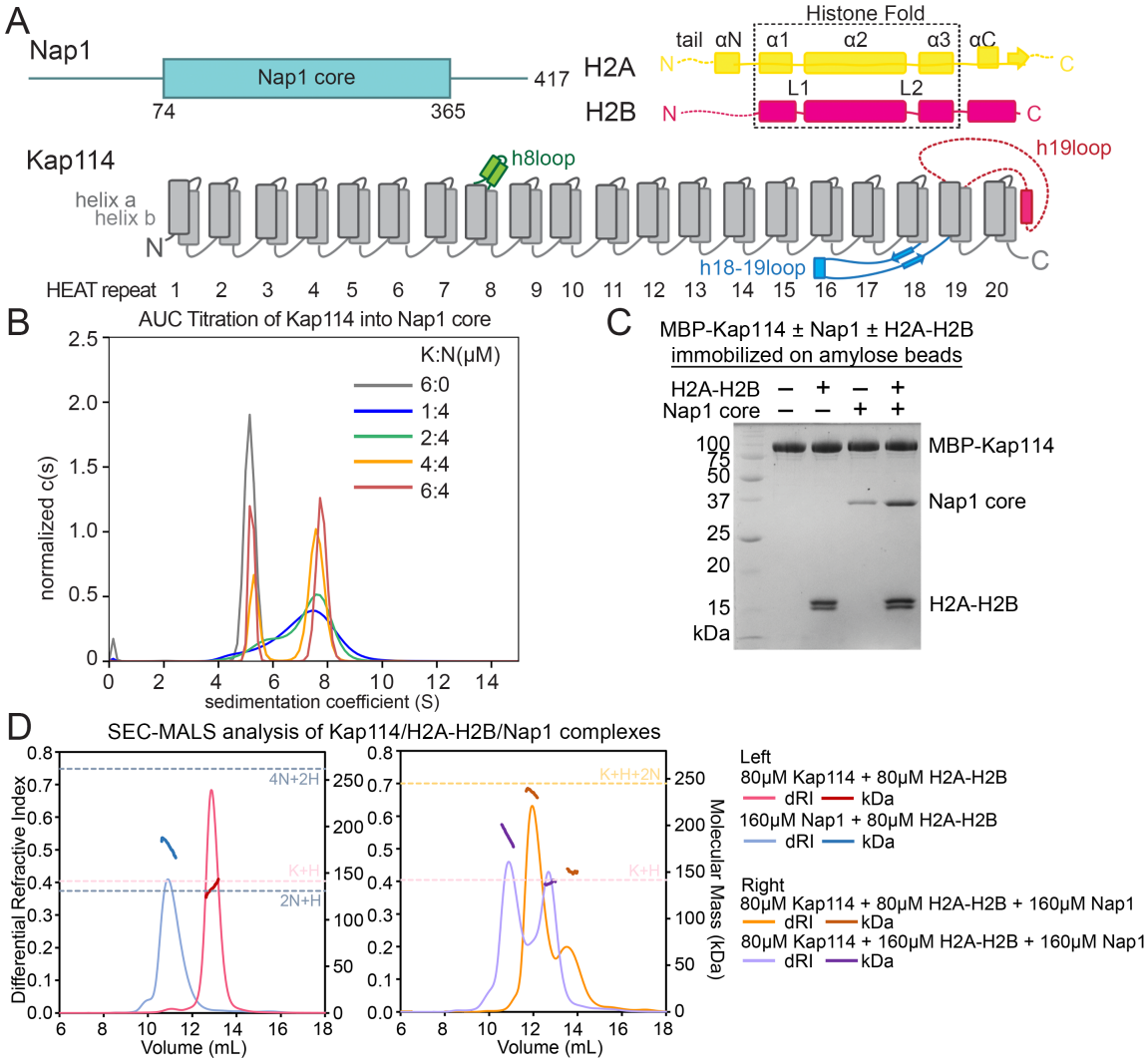


**Figure 1. Biophysical characterization of the Kap114, Nap1 and H2A-H2B complex. (A)** Domain organization of Nap1 (cyan) and schematics of H2A-H2B (yellow-pink) and Kap114 (gray, long loops labeled). **(B)** A c(s) distribution of Kap114 (5.2 S) titrating into Nap1 core to form Kap114•Nap1 complexes (7.9 S) analyzed by analytical ultracentrifugation. Molar ratios of Kap114:Nap1 (monomer concentration) used are indicated. The Kap114•Nap1 complex was estimated to have a molecular weight of 178 kDa using the c(s) distribution obtained using 6:4 (most saturated) ratio. **(C)** *In vitro* pull-down of 100 μM Nap1 core or H2A-H2B or both using 10 μM MBP-Kap114 immobilized on amylose beads. Bound proteins were visualized by SDS-PAGE and Coomassie staining. **(D)** SEC-MALS analysis of Kap114 or Nap1 binding to H2A-H2B (left) and the formation and destabilization of Kap114/H2A-H2B/Nap1 1:1:1 dimer complex without and with excess histones (right).

Nap1 C-terminal tail) also shows a large increase in apparent Kap114 affinity for Nap1 when it is pre-bound to H2A-H2B (Figure S1C). We note that Kap114-binding decreased $^{XFD488}$Nap1 FL polarization despite an apparent increase in molecular mass. This unexpected observation could be due to 1) the Kap114-bound Nap1 or Nap1•H2A-H2B complexes tumbling faster than Nap1 alone or Nap1•H2A-H2B because of their overall shapes, 2) the Nap1 tail, known to mediate self-interactions (21, 22), rotating more freely when bound to Kap114, or 3) Kap114-binding may inhibit Nap1 tetramerization (even when bound to H2A-H2B) and higher order oligomerization (23, 24) and decrease FP signal. Mass photometry of our Nap1 sample indeed shows presence of large assemblies even at the low concentration used for FP assay (Figure S1D), which may increase the Nap1 alone FP signal.

We also characterized the interactions between Kap114, Nap1 and H2A-H2B by SEC-MALS to probe the stoichiometry of the complex. Kap114 mixed with H2A-H2B (1:1 molar ratio) forms a peak that elutes at ~13 mL with a molecular mass of ~130 kDa that matches the Kap114•H2A-H2B complex (Figure 1D). Nap1 FL and H2A-H2B (molar ratio 1 Nap1 dimer:1 H2A-H2B) elutes at ~11 mL with molecular masses that span 170-200 kDa, suggesting a mixture of Nap1 dimer and tetramer with 1 or 2 H2A-H2B bound, respectively (Figure 1D). Mixing 1:1:1 molar ratio of Kap114, H2A-H2B and Nap dimer results in a peak that elutes at ~12 mL with a molecular mass of ~239 kDa, which is close to the theoretical mass of a 1:1:1 Kap114/H2A-H2B/Nap1 dimer complex (245 kDa, Figure 1D). Interestingly, when the H2A-H2B concentration is doubled (1:2:1 Kap114:H2A-H2B:Nap1 dimer ratio), we observe two peaks that match the elution profiles and molecular masses of the Nap1•H2A-H2B and Kap114•H2A-H2B controls with small

shoulders at ~10 mL and 12 mL indicating that only small populations of Kap114:H2A-H2B:Nap1 exist (Figure 1D). The results suggest that a stable assembly of one Kap114, one H2A-H2B and one Nap1 dimer is destabilized in the presence of additional free H2A-H2B.

In summary, Nap1 (full length or core) binding to Kap114 is enhanced by the presence H2A-H2B. The interactions involve one Kap114 molecule with one H2A-H2B heterodimer and one Nap1 dimer. Interestingly, this ternary complex is destabilized by the presence of excess of H2A-H2B, suggesting that the 1 Kap114/1 H2A-H2B/1 Nap1 dimer complex cannot bind addition H2A-H2B heterodimers.

**Structure determination of complexes containing Kap114, Nap1 and H2A-H2B**

Like H3-H4 biosynthesis and processing in the cytoplasm, Kap114 likely binds H2A-H2B by binding the Nap1 dimer•H2A-H2B complex (1, 7). Alignment of H2A-H2B in the Nap1•H2A-H2B (PDB: 5G2E) and Kap114•H2A-H2B (PDB: 8F0X) structures shows that the Nap1-bound H2A-H2B would clash with the N-terminal HEAT repeats of Kap114 in the Kap114•H2A-H2B structure (Figure S1E) (15, 20). Thus, it is unclear how Kap114 binds to Nap1•H2A-H2B.

We used the Nap1 core to assemble a Kap114/Nap1/H2A-H2B complex for structure determination as the Nap1 tails are disordered, flexible and seem unimportant for interactions in the complex. We prepared the cryo-EM sample by first forming a complex of Nap1 bound to *Sc* H2A-H2B (with excess histones to ensure binding), then adding Kap114 followed by 0.05% glutaraldehyde for 1 minute to stabilize the Kap114/H2A-H2B/Nap1 complexes (Figure 2A). The crosslinked complexes were

immediately separated by SEC and crosslinking efficiency of eluted fractions were evaluated by mass-photometry (Figure S2A). The crosslinked fraction enriched with Kap114, Nap1 and H2A-H2B complex(es), that also contained minimal large molecular mass aggregates, was used for cryo-EM grid preparation and data collection (Figure S2B). The cryo-EM dataset produced ~1 million particles: 38.7% are of Nap1 dimers, 36.0% Kap114•H2A-H2B, and 25.3% are ternary complexes that contain Kap114, Nap1 and H2A-H2B (Figure 2A).

Nap1 dimer particles (20.5% of all particles) were used to reconstruct a 3.2 Å resolution map (Table 1, Figure S3A). There is no density for Nap1-bound H2A-H2B in this map, consistent with the mass photometry data of the crosslinked sample (Figure S2B). Histones previously bound to Nap1 may have been stripped off during SEC or grid preparation if they were not crosslinked. We determined the structure of this unliganded Nap1 core dimer (Table 1), and it is very similar to existing Nap1 structures with only subtle differences (Figure S4). Maps obtained from Kap114•H2A-H2B particles are the same as those from binary Kap114•H2A-H2B structure (PDB: 8F0X; Figure 2A) (20).

Particles that contain Kap114, Nap1 and H2A-H2B were classified into two evenly divided classes of particles that yielded two high-resolution maps and structures. 1) A 3.2 Å resolution map showing Nap1 interacting with a Kap114•H2A-H2B complex where Nap1 contacts only the importin but not the histone (13.2% of all particles) – we termed this assembly the Nap1•Kap114•H2A-H2B complex (Table 1, Figure 2A-C and S3B). 2) A 3.5 Å resolution map showing both Kap114 and Nap1 interacting with the same H2A-H2B – we termed this complex Nap1•H2A-H2B•Kap114 (Table 1, Figure 2A, D and E and S3C). Although the overall resolution of both Nap1•Kap114•H2A-H2B and Nap1•H2A-

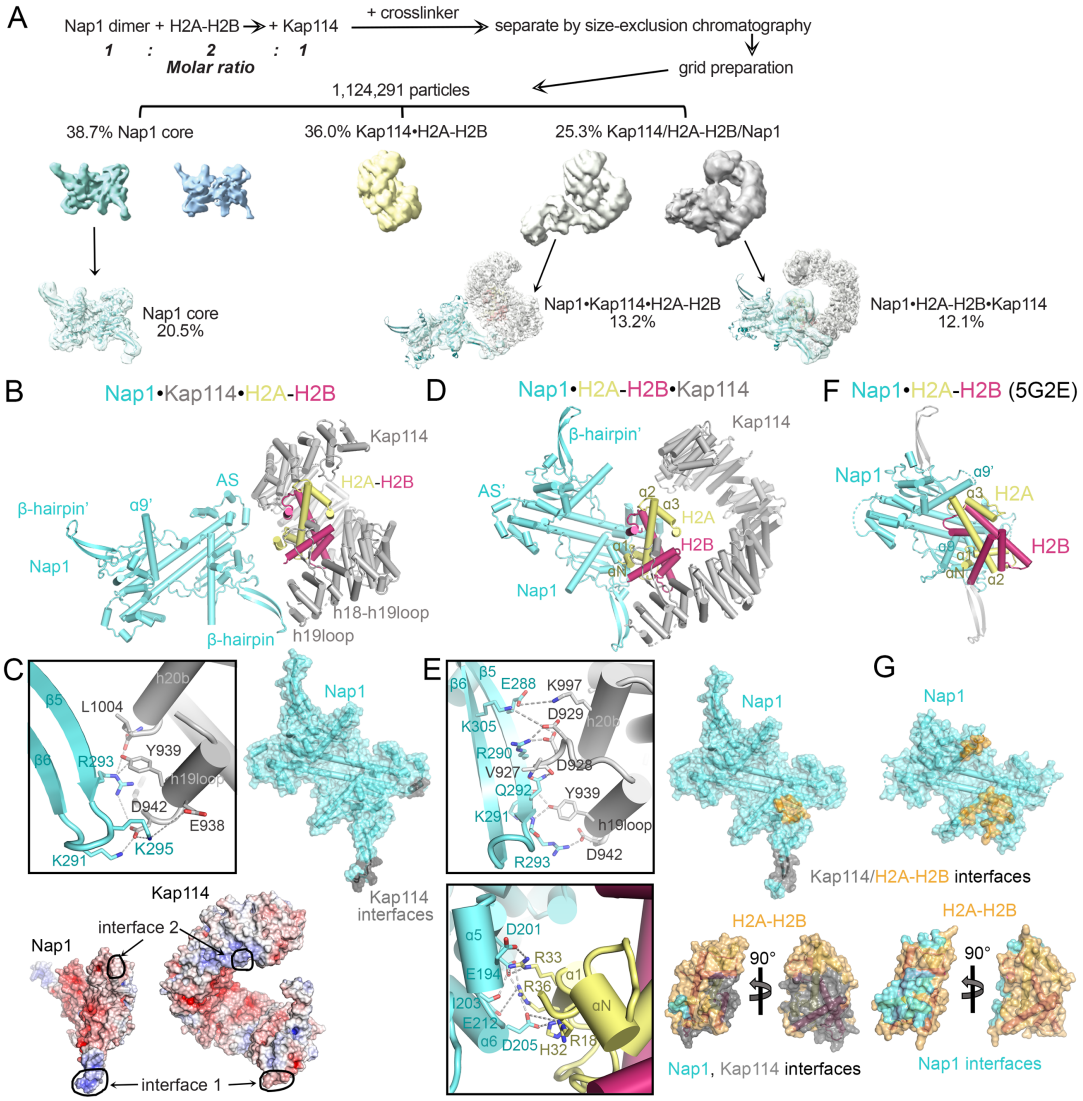


**Figure 2. Structures of two Kap114/H2A-H2B/Nap1 complexes. (A)** Schematics of cryo-EM structural determination and particle distribution in the dataset. **(B)** Nap1•Kap114•H2A-H2B structure in cyan•gray•yellow-pink respectively. **(C)** Nap1 contacts to the Kap114 h19loop (<8.0 Å in dotted lines) and the charge complementarity of the two interfaces as shown by electrostatic surface potential of Nap1 and Kap114 below (-10 to +10 ekV), rotated 90° about the vertical axis in opposite directions from the orientation in **(B)**. Kap114 interfaces on Nap1 (cyan surface with structure below) is also shown in the orientation of Nap1 in **(D)**. **(C)** Nap1•H2A-H2B•Kap114 structure colored as in **(B)**, aligned by H2A-H2B. **(E)** <8 Å contacts of Nap1 with Kap114 (top) and H2A-H2B (bottom) in boxes, and interaction interfaces (histone in orange, Kap114 in gray and Nap1 in cyan) on Nap1 (cyan) and histone (orange) surfaces in Nap1•H2A-H2B•Kap114. H2A-H2B surface on the right is shown oriented as in **(D)** on the right. **(F)** Crystal structure of Nap1•H2A-H2B (5G2E), aligned to the Nap1 in **(D)**. β-hairpins from the aligned cryo-EM Nap1 structure are in transparent light gray (alignment in Figure S4B). **(G)** Interfaces of the Nap1•H2A-H2B complex depicted in the same color and orientation as **(E)**.

H2B•Kap114 maps are ~3 Å, the densities for Nap1 are substantially worse. Local refinement improved features with local resolutions of ~6-9 Å, and we docked the Nap1 dimer and H2A-H2B cryo-EM structures into the densities (Figure S3B, C and S5).

**Structure of the Nap1•Kap114•H2A-H2B complex**

The Nap1•Kap114•H2A-H2B structure shows Kap114 wrapping around H2A-H2B while the Nap1 dimer binds Kap114 without interacting with H2A-H2B (Figure 2D). Kap114 in this complex adopts the same conformation as in the binary Kap114•H2A-H2B complex (PDB: 8F0X; root mean square deviation or RMSD < 0.5 Å, Figure S6A), where N- and C-terminal HEAT repeats (h2-h5 and h17-h19) interact with the H2A-H2B core (Figure 2B, interfaces in Figure S7) (19, 20).

Kap114 uses two distant interfaces, at the basic h6-h7loop and a helix within the acidic h19loop (residues 931-942, previously unmodeled (19, 20)), to contact Nap1 (Figure 2B). The h6-h7loop is close to the Nap1 accessory subdomain (AS) even though the AS cannot be confidently modeled due to poor density (Figure S5A). The proximity of Nap1 to Kap114 here is likely stabilized by electrostatic complementarity from multiple negatively charged Nap1 AS residues and basic side chains in the Kap114 h6-h7 loop (Figure 2D). The other Kap114-Nap1 interface involves the acidic Kap114 h19loop binding the basic Nap1 β-hairpin (Figure 2D), consistent with previous mutagenesis of Nap1 residues 290-295 in the β-hairpin abolishing Kap114-Nap1 interactions (15). We show that removal of the Kap114 h19loop (Kap114Δh19loop) has the same effect (Figure S1F), consistent with previous reports that the C-terminal 107 residues of Kap114 (includes h19loop, h19b, h20a and h20b) are necessary for Nap1-binding (25). A

reconstructed Small Angle X-Ray Scattering (SAXS) envelope of the binary Kap114•Nap1 complex is consistent with the Kap114-Nap1 arrangement in Nap1•Kap114•H2A-H2B (Figure S8), suggesting that this mode of Kap114-Nap1 interaction can occur with or without H2A-H2B and that it is not an artifact of crosslinking in the cryo-EM sample. Together, the new and old results reveal that Kap114 h19loop and Nap1 β-hairpin constitute the binding hot spot in the absence of H2A-H2B.

The H2A-H2B binding site of Nap1 in the Nap1•Kap114•H2A-H2B is not occluded but there is no density for a Nap1-bound H2A-H2B. This observation is consistent with our finding that a complex of one Kap114 bound to one H2A-H2B one Nap1 dimer is stable but additional H2A-H2B destabilized the assembly. It is possible that H2A-H2B binding to Kap114-bound Nap1 causes allosteric changes to Nap1 that renders Kap114-Nap1 interactions unfavorable or a H2A-H2B bound to this Nap1 that was not crosslinked was stripped off during SEC.

**Structure of the Nap1•H2A-H2B•Kap114 complex**

The Nap1•H2A-H2B•Kap114 complex revealed pairwise interactions between the three proteins, distinct from the Nap1•Kap114•H2A-H2B complex (Figure 2C). Here, H2A-H2B is sandwiched between the Nap1 dimer and the C-terminal HEAT repeats of Kap114. Interactions between the C-terminal Kap114 repeats and H2A-H2B interaction are similar in all structures where Kap114 binds H2A-H2B (PDB: 8F0X and 8F1E) (20) (Figure S7, center and right). However, in the Nap1•H2A-H2B•Kap114 complex, the N-terminal half of Kap114 adopts an open conformation with repeats h1-h2 far from the bound H2A-H2B (~20 Å), even farther than the ~10 Å distance in the recently reported

RanGTP•Kap114•H2A-H2B structure (PDB: 8F1E) (Figure S7, left) (20, 26). Conformational differences of the N-terminal repeats h1-h5 of Kap114 in Nap1•H2A-H2B•Kap114 vs Nap1•Kap114•H2A-H2B arise from differences in orientations between individual repeats, while the remaining repeats (h6-h20) rearrange due to two hinges at h13-14 and h16-h17 (Figure S6B), which are also key for conformational changes involved in RanGTP-binding (20).

Nap1 in the Nap1•H2A-H2B•Kap114 complex is tethered at two sites, one to Kap114 and another to H2A-H2B. The Kap114-Nap1 interface involves the Nap1 β-hairpin contacting the Kap114 h19loop and h20b helix through multiple potential electrostatic and polar interactions (Figure 2E, top box). This interface is larger than the similar interface in Nap1•Kap114•H2A-H2B but the Nap1 β-hairpin of Nap1•H2A-H2B•Kap114 is pivoted/rotated at its end so that Nap1 is closer to Kap114 and H2A-H2B.

The Nap1-histone interface involves a few acidic residues in the Nap1 α4-6 helices that are likely making electrostatic interactions with a few basic residues of the H2A αN and α1 helices (Figure 2E, bottom box). This interface (207 $Å^2$) in Nap1•H2A-H2B•Kap114 is ~1/4 of the histone interface of the binary Nap1•H2A-H2B complex (PDB: 5G2E, 814 $Å^2$) (Figure 2F and G) (17). Comparing Nap1•H2A-H2B•Kap114 with Nap1•H2A-H2B, the H2A-H2B in the former appears to maintain a small foothold on Nap1 as it pivots about this interface away from Nap1 to bind Kap114 (Figure 2C, E, G). It is thus unlikely for Nap1 to bind another H2A-H2B when bound in this Nap1•H2A-H2B•Kap114, again consistent with our finding that Kap114, H2A-H2B and the Nap1 dimer form a 1:1:1 complex. Previous work reported that mutations of the Nap1 β-hairpin

residues 290-292 abolished Kap114-binding when no H2A-H2B was present, but binding was partially restored by adding chicken histones (15). This is consistent with the structure revealing this Nap1-H2A-H2B interface, which may maintain the Nap1•H2A-H2B•Kap114 complex when the Nap1 β-hairpin-Kap114 h19loop interface is lost.

**Nap1 and H2A-H2B are both chaperoned when bound to Kap114**

The Nap1•Kap114•H2A-H2B and Nap1•H2A-H2B•Kap114 structures reveal how Kap114 chaperones both Nap1 and H2A-H2B. Nap1 is prone to tetramerization/oligomerization and H2A-H2B binding to Nap1 does not seem to change this propensity (Figure 1D). However, all our biochemical and structural data show one Kap114 binding to only one Nap1 dimer and not any high order oligomer of Nap1 (Figure 1B, S1B and S8). Nap1 tetramerization was suggested to occur in two ways: 1) two Nap1 dimers form ring-like tetramers through electrostatic interactions between the positively charged β-hairpins and the negatively charged ASs (27) or 2) the β-hairpins stack in an amyloid-like manner (18). Kap114 binding to the β-hairpin and AS of Nap1 in the Nap1•Kap114•H2A-H2B complex sequesters both elements from participating in interactions between Nap1 dimers to form Nap1 tetramers/oligomers (Figure 2B). Similarly, the Nap1 the β-hairpin and AS are also inaccessible for Nap1 oligomerization in the Nap1•H2A-H2B•Kap114 complex as the Nap1 β-hairpin interacts with Kap114 and the AS is positioned only 17 Å away from the h5-h6 loop of Kap114 and is likely inaccessible (Figure 2D).

It is well established that Nap1, as well as Kap114 and its *Hs* homolog Imp9, are

very effective histone chaperones of H2A-H2B; all three proteins prevent aggregation of H2A-H2B with DNA (9-12, 20, 26). Not surprisingly, in both Nap1•Kap114•H2A-H2B and Nap1•H2A-H2B•Kap114 complexes, the histone and DNA binding regions of H2A-H2B are well chaperoned (Figure S9). In Nap1•H2A-H2B•Kap114, Kap114 and Nap1 together buries a large area of ~1762 $Å^2$ on H2A-H2B, approximately 10% more than the H2A-H2B surface buried by Nap1 alone (814 $Å^2$). In Nap1•Kap114•H2A-H2B, Kap114 chaperones H2A-H2B extensively in the same way as in the binary Kap114•H2A-H2B complex (PDB: 8F0X) (20), where Kap114 alone buries ~2206 $Å^2$ of H2A-H2B.

**Structural basis of H2A-H2B enhancing Kap114-Nap1 binding**

The Nap1•Kap114•H2A-H2B and Nap1•H2A-H2B•Kap114 structures also explain how H2A-H2B enhances Nap1-Kap114 binding (Figure 1C and S1C). Nap1 density in the Nap1•Kap114•H2A-H2B map is weak, suggesting that the Kap114-Nap1 interactions at the two small interfaces are dynamic (Figure S3B). The unliganded Kap114 superhelix, like all karyopherin superhelices, is flexible and likely samples multiple conformations. Kap114 binding to Nap1 alone is likely not strongly favored over Nap1 tetramerization and is thus of weak affinity.

Comparison of the Kap114 conformations in Nap1•Kap114•H2A-H2B vs unliganded Kap114 (PDB: 6AHO) shows structural rearrangement of Kap114 (hinge at h16-h17) as H2A-H2B-binding stabilizes the most compact conformation of the Kap114 superhelix observed thus far (83 Å *versus* 95 Å distance between h9-h10loop and h17-h18loop) (Figure S6C). The Kap114 N- and C-termini of Nap1•Kap114•H2A-H2B are close and therefore favorable for interacting with both the Nap1 β-hairpin and AS (Figure

2B and C). The Kap114 conformation in Nap1•H2A-H2B•Kap114 is much more extended than Kap114•H2A-H2B or even unliganded Kap114, but the Nap1 dimer is bought closer to the Kap114 h19loop by its interaction with the H2A-H2B that is bound to C-terminal h17-h19 repeats of Kap114 (Figure 2D and E, S6C). Kap114-Nap1 binding in Nap1•H2A-H2B•Kap114 is likely stabilized by direct and indirect (via H2A-H2B) Kap114-Nap1 interactions.

The Nap1•Kap114•H2A-H2B and Nap1•H2A-H2B•Kap114 populations are evenly distributed in our cryo-EM dataset (Figure 2A). The two distinct assemblies may exist in equilibrium with both complexes contributing to increased Kap114-Nap1 affinity when H2A-H2B is present. Alternatively, the cryo-EM sample is crosslinked and Nap1•H2A-H2B•Kap114 may instead be an intermediate that is captured as Kap114 binds the pre-formed Nap1•H2A-H2B complex and H2A-H2B is in mid-transfer from Nap1 to Kap114. However, we cannot discern the two possible scenarios at this time. If H2A-H2B is being transferred, we also cannot discern the direction of transfer. Further kinetic experiments are needed to elucidate the true contribution of the two different structural arrangements of the Kap114/Nap1/H2A-H2B complexes. Regardless, structural and biophysical analyses suggest that Nap1 is unlikely to be imported by Kap114 to the nucleus alone. Instead, the Nap1 dimer is co-imported along with a H2A-H2B heterodimer, by Kap114. It is unclear from the structures which complex, Nap1•Kap114•H2A-H2B or Nap1•H2A-H2B•Kap114, is more suitable for translocation across the nuclear pore complex (NPC). H2A-H2B is most shielded in Nap1•Kap114•H2A-H2B (Figure S9) and therefore more protected for its passage across the hydrophobic central transport channel of the NPC but future studies are needed to test this hypothesis.

**The effects of RanGTP on H2A-H2B- and Nap1-binding to Kap114**

RanGTP usually binds with high affinity to importins and dissociates the importin•cargo complex to release the cargo in the nucleus. H2A-H2B import is an exception where RanGTP binds Kap114•H2A-H2B to form a stable ternary RanGTP•Kap114•H2A-H2B complex (20). We performed AUC analysis and found that Kap114-Nap1 interaction also persists in the presence of RanGTP (Figure S10A).

A previous report suggested that interactions between Kap114, Nap1 and H2A-H2B were not disrupted by RanGTP (15). We used SEC-MALS to assess the stability of the quaternary Kap114/Nap1/H2A-H2B/RanGTP complex(es) (Figure 3A). As shown earlier, the 1 Kap114:1 H2A-H2B:1 Nap1 dimer mixture produced a major peak that matched the ternary complex(es) and a smaller peak (eluted immediately after the major peak; molecular mass ~150 kDa) that is likely a mix of several smaller species resulting from dissociation of the ternary complexes (Figure 3A). When RanGTP is added in 1:1 molar ratio to the 1 Kap114:1 H2A-H2B:1 Nap1 dimer mixture, the major peak shifts to ~10.5 mL with a molecular mass of 270-293 kDa, consistent with the formation of Kap114/Nap1/H2A-H2B/RanGTP complexes (theoretical mass of the 1:1:1:1 RanGTP:Kap114:H2A-H2B:Nap1 dimer complex is 269 kDa). A minor peak with ~150 kDa molecular mass also eluted immediately after the major peak, but its lower DRI suggests that RanGTP stabilizes the Kap114/H2A-H2B/Nap1 complexes and less dissociated components are observed in the SEC.

We used FP assays to probe Kap114-H2A-H2B or -Nap1 binding affinities to better characterize the effect of RanGTP in an equilibrium assay. Titrations of Kap114 or Kap114:RanGTP (1:1 molar ratio) into XFD488-labeled H2A-H2B show that RanGTP

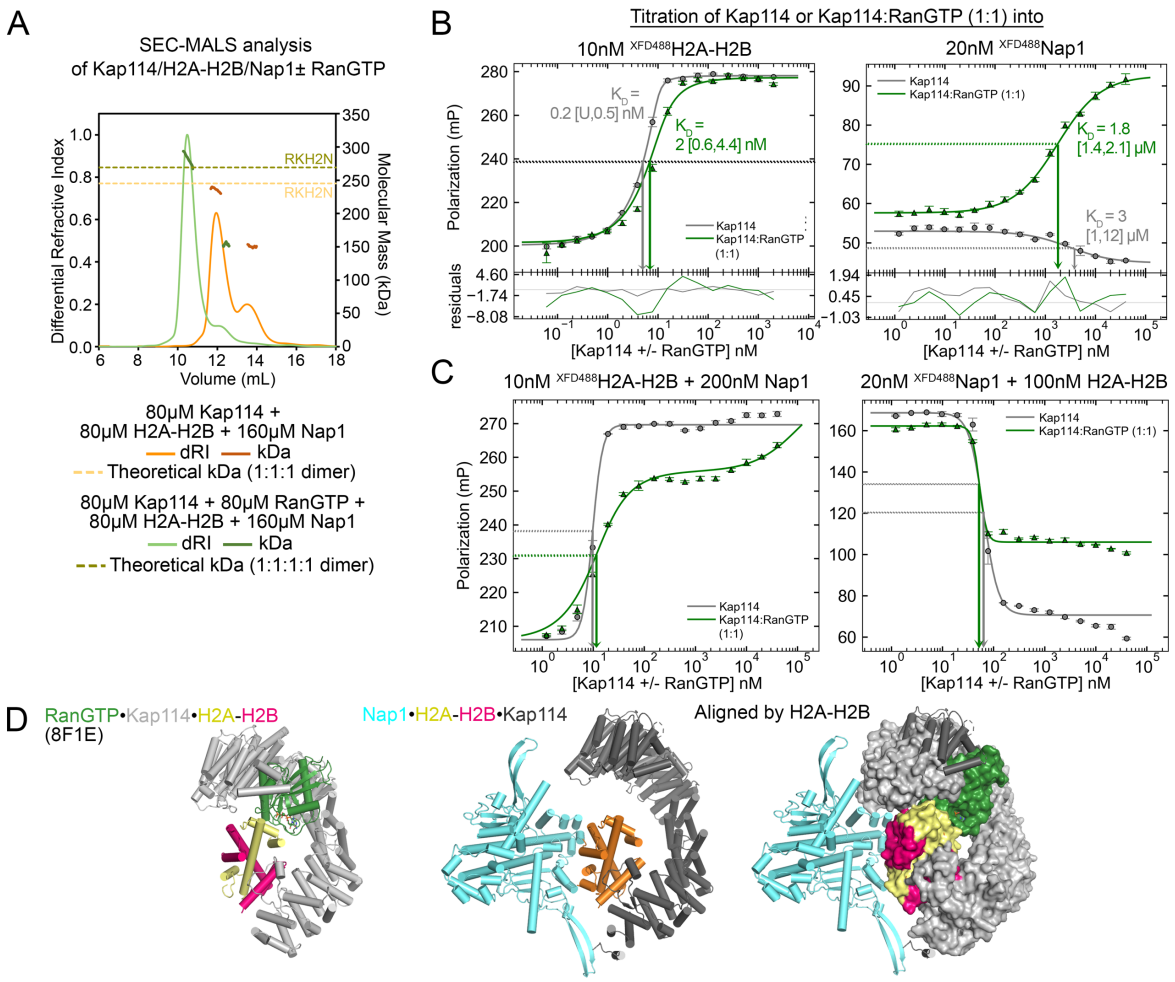


**Figure 3. Probing the effect of RanGTP on Kap114/H2A-H2B/Nap1 interactions.** **(A)** SEC-MALS analysis of the formation of quaternary Kap114 (K), Nap1 FL dimer (2N), H2A-H2B (H) and RanGTP (R) complex. The traces from the sample without RanGTP is a replicate of Figure 1D. **(B)** FP titrations of Kap114 or Kap114:RanGTP (1:1) into 10 nM $^{XFD488}$H2A-H2B/Nap1 FL. Data points are mean ± s.d. of triplicate measurement and fitted with 1-site binding model (lines). Residuals from fitting are plotted below and dissociation constants ($K_D$ [95% confidence interval]) are displayed. ~50% binding is indicated by dotted line and arrow to show $K_D$. **(C)** As in **(B)**, but Kap114 or Kap114:RanGTP were titrated into Nap1•H2A-H2B complexes where the unlabeled protein was used in 10X molar excess to ensure 100% binding. Lines here are not meaningful fits and are shown for visual guidance only. **(D)** Alignment of H2A-H2B from RanGTP•Kap114•H2A-H2B (in green•light gray•yellow-red; PDB ID: 8F1E) and Nap1•H2A-H2B•Kap114 (in cyan•orange•dark gray). The Nap1 does not clash with RanGTP bound Kap114 but is positioned so that Nap1 AS is in close proximity with RanGTP-bound Kap114 (in surface on the right).

decreases the Kap114-H2A-H2B affinity by ~10-fold, from 0.2 [U,0.5] nM to 2 [0.6,4.4] nM (Figure 3B, left). In contrast, similar experiments with XFD488-labeled Nap1 show a slight increase of the Kap114-Nap1 affinity in the presence of RanGTP from 3 [1,12] μM to 1.8 [1.4,2.1] μM (Figure 3B, right). The same trend was observed when $^{XFD488}$H2A-H2B was first incubated with excess Nap1 or $^{XFD488}$Nap1 was first incubated with excess H2A-H2B (Figure 3C). The affinity of Kap114 for Nap1-bound $^{XFD488}$H2A-H2B•Nap1 is decreased when RanGTP is present (Figure 3C, left). Conversely, the affinity of Kap114 for H2A-H2B-bound $^{XFD488}$Nap1 increases slightly when RanGTP is present (Figure 3C, right). Therefore, our results show that RanGTP decreases Kap114-H2A-H2B affinity but strengthens Kap114-Nap1 binding, and this effect is not affected by the presence of Nap1 or H2A-H2B respectively.

**Models of nuclear assemblies of Nap1, H2A-H2B, Kap114 and RanGTP**

We explored aligning the histones of either Nap1•Kap114•H2A-H2B or Nap1•H2A-H2B•Kap114 with RanGTP•Kap114•H2A-H2B (PDB: 8F1E) to generate models of nuclear RanGTP•Kap114•H2A-H2B•Nap1 quaternary complexes (20). We first aligned the H2A-H2B heterodimers of Nap1•Kap114•H2A-H2B and RanGTP•Kap114•H2A-H2B to position Nap1 of the former onto the latter. Nap1 is placed such that there is only one Nap1 interface, of the Nap1 β-hairpin binding to the Kap114 h19loop, in contrast to two Nap1 interfaces in the Nap1•Kap114•H2A-H2B or Nap1•H2A-H2B•Kap114 complexes (Figure S10B). The smaller Kap114-Nap1 interface in the model is inconsistent with the increased Kap114-Nap1 affinity in the presence of RanGTP observed in FP analysis (Figure 3B).

In contrast, alignment of the H2A-H2B heterodimers in Nap1•H2A-H2B•Kap114 and RanGTP•Kap114•H2A-H2B places Nap1 such that in addition to Nap1 contacting H2A-H2B, its AS binds the Kap114 h6loop (no observed charge repulsion nor steric clash) and its β-hairpin binds the Kap114 h19loop (Figure 3D and S10C). This quaternary RanGTP•Kap114•H2A-H2B•Nap1 model, with additional Nap1-binding interfaces with Kap114, is consistent with the FP finding that Nap1 affinity is enhanced (Figure 3B). Interestingly, in light of the previous report that mutating Nap1 β-hairpin residues 290-292 resulted in RanGTP disrupting the ability of mutant Nap1 to pull-down Kap114 and H2A-H2B (15), we suggest that contribution of the Nap1-Kap114 h19loop interface to total binding is more significant when RanGTP is present; whereas when RanGTP is absent, the Nap1-Kap114 h19loop interface is dispensable.

It is however unclear how stabilization of Kap114-Nap1 interactions in the Nap1•H2A-H2B•Kap114 complex by RanGTP fits into the next steps of H2A-H2B deposition in nucleosome assembly. FP analysis shows that Kap114-H2A-H2B affinity is decreased by RanGTP, albeit to a lesser degree when Nap1 is present (Figure 3B and C). The decreased affinity is likely due to exposure of the DNA-binding region of H2A-H2B when RanGTP binds Kap114 in the RanGTP•Kap114•H2A-H2B (PDB: 8F1E). This H2A-H2B surface remains exposed in the RanGTP•Kap114•H2A-H2B•Nap1 model, but the increase in dissociation rate caused by the exposure may be dampened by H2A-H2B interactions with Nap1 (Figure 3D). Such an assembly is likely still suitable to deposit H2A-H2B to the assembling nucleosome. Alternatively, H2A-H2B may be handed back to Nap1 for transfer to the assembling nucleosome or to another nuclear histone chaperone.

**A model for H2A-H2B and Nap1 co-import by Kap114**

Based on the biophysical and structural results presented, we propose a model for the co-import of H2A-H2B and Nap1 to Kap114. To discuss how Nap1•H2A-H2B might encounter Kap114, we must first consider the initial or most likely H2A-H2B binding site on Kap114. The common H2A-H2B binding site in the five available structures of importin-bound H2A-H2B complexes (Imp9•H2A-H2B, Kap114•H2A-H2B, RanGTP•Kap114•H2A-H2B and described here, Nap1•Kap114•H2A-H2B and Nap1•H2A-H2B•Kap114) is at the C-terminal HEAT repeats of Kap114/Imp9 (20, 26). This interface is also the larger of the two importin•H2A-H2B interfaces (1438 $Å^2$ *vs* 752 $Å^2$ for C- and N-terminal sites, respectively). These two factors suggest that the C-terminal importin interface is most likely the primary H2A-H2B binding site. This interface on H2A-H2B does not contact Nap1 and thus is fully accessible in the Nap1•H2A-H2B complex to bind Kap114 (Figure 2E and G). It is therefore likely that Nap1•H2A-H2B encounters Kap114 via initial contact of H2A-H2B with the C-terminal H2A-H2B-binding site of Kap114, especially with the h18-19loop of Kap114, which is disordered and flexible in the unliganded importin. Such an encounter complex may approximate the model of Nap1•H2A-H2B superimposed onto the H2A-H2B of Nap1•H2A-H2B•Kap114 (Figure 4A).

It is unclear if the encounter assembly would then rearrange to take on the structure of Nap1•Kap114•H2A-H2B or Nap1•H2A-H2B•Kap114 for translocation across the NPC (Figure 4B). Regardless, since Nap1 alone binds to Kap114 with such low affinity, it is unlikely that Nap1 will be imported without H2A-H2B whereas it was previously shown that H2A-H2B can be imported into the nucleus without Nap1 (14). We

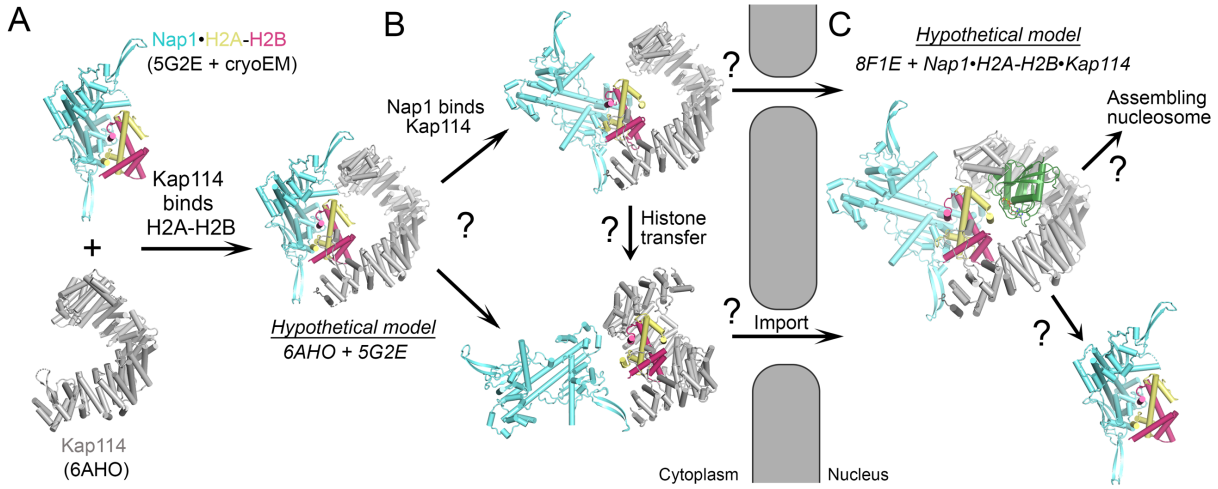


**Figure 4. Proposed model of Kap114 co-import of H2A-H2B and Nap1. (A)** After synthesis by ribosomes and folding, H2A-H2B is likely chaperoned by Nap1 when it encounters unliganded Kap114. In the initial encounter, Kap114 likely uses its C-terminal HEAT repeats to engage the histones in Nap1•H2A-H2B (hypothetical encounter model generated by aligning Nap1•H2A-H2B structure, 5G2E with the β-hairpin from cryo-EM structure from this study, to H2A-H2B of Nap1•H2A-H2B•Kap114. **(B)** Histones can be transferred to Kap114 from Nap1 and form two ternary complexes with different arrangements, but it is unclear which or whether both ternary complexes are amenable for crossing the nuclear pore to enter the nucleus. **(C)** When RanGTP binds to this complex in the nucleus, H2A-H2B is no longer chaperoned by the N-terminus of Kap114, likely in a hypothetical model generated by aligning Nap1•H2A-H2B•Kap114 to H2A-H2B of RanGTP•Kap114•H2A-H2B (8F1E). The histone can be transferred back from Kap114 to Nap1 or other unknown nuclear chaperones or be deposited into assembling nucleosome.

also found that excess H2A-H2B will destabilize the Kap114, H2A-H2B and Nap1 containing import complex(es) and dissociate the Kap114-Nap1 interaction. This may ensure that Nap1 is always available in the cytoplasm to chaperone any free H2A-H2B.

When a complex that contains Kap114, Nap1 and H2A-H2B enters the nucleus, it binds RanGTP because Kap114-H2A-H2B affinity remains high in the presence of the GTPase and RanGTP-binding does not decrease Kap114-Nap1 affinity (Figure 3B). However, RanGTP-binding likely modulates H2A-H2B interactions to expose part of the histone surface as in the RanGTP•Kap114•H2A-H2B complex (20). We generated a

reasonable model of the quaternary RanGTP•Kap114•H2A-H2B•Nap1 complex by aligning the histones in the RanGTP•Kap114•H2A-H2B (PDB 8F1E) and Nap1•H2A-H2B•Kap114 structures (Figure 3D and 4C). Even though H2A-H2B in this complex is more exposed and poised to leave, it is unclear where it will go. Is it handed back to Nap1 in the quaternary complex, to other nuclear chaperones or to the assembling nucleosome? However, once H2A-H2B dissociates from Kap114, Nap1 will likely also be released as the Kap114-Nap1 and RanGTP-Kap114-Nap1 affinities are weak when H2A-H2B is not present.

To summarize, we found that one Kap114 a binds Nap1 dimer stoichiometry, and their interaction is enhanced by H2A-H2B-binding to form complexes with two distinct arrangements, as revealed by cryo-EM structure determination. The structures explain how Kap114 chaperones both Nap1 and H2A-H2B, as well as how H2A-H2B binding increases the affinity of the previously weak Kap114-Nap1 interaction by direct interactions with both proteins and by stabilizing a Kap114 conformation for optimal interactions with Nap1. RanGTP further enhances Nap1 binding to Kap114-H2A-H2B, while conferring negative cooperativity with H2A-H2B binding to Kap114 within a nuclear quaternary RanGTP•Kap114•H2A-H2B•Nap1 complex that we modeled from two different cryo-EM structures. Further studies are necessary to determine the structure of the RanGTP•Kap114•H2A-H2B•Nap1 complex and to delineate the downstream steps leading to H2A-H2B deposition into the assembling nucleosome.

## Materials and Methods

### Protein constructs, expression, and purification

Kap114 was cloned into two modified vectors: pGEX-4T3 (Cytiva) and pMalE (New England BioLabs). pGEX-4T3 was modified to insert a TEV cleavage site between the GST tag and Kap114 whereas pMalE was modified to insert a $His_6$-tag immediately N-terminus of MBP and a TEV cleavage site after the MBP. Both Kap114 constructs were expressed and purified as previously described (20). Nap1 FL (C200A, C249A, C272A mutation for specific labeling on 414C) cloned into a pHAT4 vector was a gift from Sheena D'Arcy. The Nap1 core (residues 75-365) cloned into a pET15b vector was a gift from Karolin Luger. Both Nap1 proteins were expressed and purified as previously described (21). Lyophilized *Sc* and *Xl* histones were obtained from The Histone Source and refolded according to established protocol (16).

### Pull-down binding Assays

*In vitro* pull-down binding assays were performed as previously described (28). In brief, 10 μM of MBP-Kap114 was immobilized on amylose resin (New England Biolabs) and incubated with either 100 μM *Xl* H2A-H2B, 100 μM Nap1 (monomer concentration), or both H2A-H2B and Nap1. These samples were then washed three times with buffer and bound proteins were separated and visualized by SDS-PAGE gel stained with Coomassie stain.

### Analytical Ultracentrifugation

Sedimentation velocity experiments were performed as previously described (26). Individual proteins were dialyzed into Analytical Ultracentrifugation (AUC) buffer

containing 20 mM Tris-HCl pH 7.5, 150 mM NaCl, 2 mM $MgCl_2$ and 2 mM TCEP. 500 µL of AUC sample was equilibrated overnight at 4°C. The AUC sample chamber contained 400 µL of the following: 1) 6 µM Kap114, 2) 1 µM Kap114 + 4 µM Nap1 core, 3) 2 µM Kap114 + 4 µM Nap1 core, 4) 4 µM Kap114 + 4 µM Nap1 core, 5) 6 µM Kap114 + 4 µM Nap1 core. Nap1 concentrations are that of monomers. In another experiment, the AUC chamber contained 400 µL of 1) 3 µM Kap114, 2) 3 µM RanGTP, 3) 0.75 µM Nap1 core dimer, 3 µM Kap114 + 0.75 µM Nap1 core dimer, and 3 µM Kap114 + 0.75 µM Nap1 core dimer + 3 µM RanGTP. Sedimentation coefficients were measured by monitoring absorbance at 280 nm in a Beckman-Coulter Optima XL-1 Analytical Ultracentrifuge. The Beckman data time stamps were corrected using REDATE (29). SEDNTERP was used to calculate the buffer density, buffer viscosity, and protein partial-specific volumes (30). SEDFIT was used to calculate sedimentation coefficient distributions c(*s*) where the regularization calculated a confidence level of 0.68 was used, time-independent noise elements were accounted for, and at a resolution of 100 (31). SEDFIT was also used to estimate molecular weight by obtaining the sedimentation coefficient through integration of c(*s*) and the frictional ratios by refining the fit of the model. The c(*s*) distribution and isotherm integration was done with GUSSI (32). Further isotherm fitting was performed using SEDPHAT (33).

**Fluorescence Polarization**

*Xl* H2A (K119C) was labeled with XFD488 (ATT Bioquest) in a 1:4 molar ratio under denaturing conditions for 3 hours before refolding with *Xl* H2B. Nap1 FL was also labeled with XFD488 in 1:4 molar ratio after nickel affinity purification (Qiagen) and further

purified with anion exchange and size exclusion chromatography (Cytiva). All other proteins were dialyzed in buffer containing 20 mM HEPES pH 7.4, 150 mM NaCl, 2 mM $MgCl_2$, 10% glycerol (v/v) and 2 mM TCEP overnight before use. Fluorescence polarization assays were performed as previously described in the same buffer (34). In brief, triplicates of sixteen 20 µL samples were assembled with indicated concentrations in a 384 well black bottom plate (Corning). Measurements were performed in a CLARIOstar Plus plate reader (BMG Labtech) with top optics using excitation filter 482-16, dichroic filter LP 504 and emission filter 530-40, 50 flashes per well. Gain was optimized to target mP of ~ 200 for $^{XFD488}$H2A-H2B and ~ 184 for $^{XFD488}$Nap1•H2A-H2B (to match the value found when gain was optimized for $^{XFD488}$H2A-H2B). Data was analyzed in PALMIST (35) and plotted in GUSSI.

**Size Exclusion Chromatography Multi-Angle Light Scattering**

Size Exclusion Chromatography Multi-Angle Light Scattering (SEC-MALS) experiments were performed with 20 mM HEPES pH 7.4, 150 mM NaCl, 2 mM $MgCl_2$, and 2 mM TCEP. Sample dialysis, buffer filtration, and SEC-MALS experiments were done following established protocol (21). To verify the stoichiometry of Nap1 FL bound to Kap114 the following samples were analyzed: 80 µM Kap114, 160 µM Nap1 FL (monomer), 80 µM Kap114 + 160 µM Nap1, 80 µM Kap114 + 80 µM *Xl* H2A-H2B, 160 µM Nap1 + 80 µM *Xl* H2A-H2B, 80 µM Kap114 + 160 µM Nap1 + 80 µM *Xl* H2A-H2B, 80 µM Kap114 + 160 µM Nap1 + 160 µM *Xl* H2A-H2B, 80 µM Kap114 + 160 µM Nap1 + 80 µM RanGTP, and 80 µM Kap114 + 160 µM Nap1 + 80 µM *Xl* H2A-H2B + 80 µM RanGTP.

**Mass Photometry**

Mass photometry data was acquired using a TwoMP mass photometer (Refeyn). The laser was warmed up for an hour before use. During that waiting period, the glass slide was washed by alternating between Milli-Q filtered water, isopropanol, and then Milli-Q water, twice. A 2 by 4 strip of wells were adhered to the middle of the glass slide. Immersion oil was applied onto the lens before placing the glass slide on top. Prior to the measurement, 2 mg/mL BSA was diluted 100-fold with freshly filtered buffer from either FP assay (for $^{XFD488}$Nap1) or cryo-EM complex running buffer (for crosslinked cryo-EM sample – details below). BSA was used for generating the calibration curve, using an additional 10-fold dilution: we first added 16.2 µL of buffer into a well and brought it to focus then mixed in 1.8 µL of BSA and 60 s movies were recorded. The $^{XFD488}$Nap1 data were collected at final concentration of 20, 10, and 5 nM while crosslinked cryo-EM fractions were diluted to under 7000 counts for collection in a similar manner as the BSA. Data was processed through Gaussian fitting to provide the peak mass and relative populations using the Refeyn analysis software.

**Cryo-EM sample preparation and data collection**

*Sc* H2A-H2B, Nap1, and Kap114 were dialyzed overnight into cryo-EM buffer containing 20 mM Tris pH 7.5, 150 mM NaCl, and 2 mM DTT. 1:2 molar ratio of Nap1 core dimer:H2A-H2B heterodimer was pre-equilibrated at room temperature for 10 minutes. Then, 1 molar ratio of Kap114 was mixed in, followed by rapid addition of glutaraldehyde to a final concentration of 0.05%. Crosslinking proceeded for one minute before quenching and removal of glutaraldehyde size exclusion chromatography using a Superdex200 10/300 Increase column (Cytiva) that was previously equilibrated with

buffer containing 20 mM Tris pH 7.5, 150 mM NaCl, and 2 mM TCEP. 0.5 mL fractions were collected and analyzed using a Refeyn Mass Photometer as described above. Fraction A8, which contained the least aggregated species and most enriched with complex that likely contains Nap1, Kap114 and H2A-H2B (described in main text and Supplementary Fig. S2) was selected or cryo-EM grid preparation. The ~2.4 mg/mL protein sample was diluted two-fold with cryo-EM buffer and supplemented with Triton X-100 to a final concentration of 0.003125% (w/v). Cryo-EM grids were glow-discharged, blotted, and plunge-frozen as previously described (28).

A 48-hour data collection with the best grid was performed at the UT Southwestern Cryo-Electron Microscopy Facility on a Titan Krios microscope (Thermo Fisher) at 300 kV with a Gatan K3 detector in correlated double sampling super-resolution mode at a magnification of 105,000X corresponding to a pixel size of 0.415 Å. A total of 10,806 movies were collected; each movie was recorded for a total of 60 frames over 5.4 s with an exposure rate of 7.8 electrons/pixel/s. The datasets were collected using SerialEM software (36) with a defocus range of -0.9 and -2.4 μm.

**Cryo-EM data processing and structure determination**

Cryo-EM data was processed using cryoSPARC (37). The movies were subjected to Patch Motion Correction (binned twice) and Patch CTF Estimation. Training particles were obtained by blob picking on 100 micrographs and followed by 2D classification of the particle stack. Particles containing Kap114 were used to train on Topaz (38) which picked 665,443 particles. These particles were subjected to three rounds of 2D classification (300 classes/run). 113,471 particles that contained both Kap114 and Nap1

were split into two Ab-initio classes, the Nap1•H2A-H2B•Kap114 and Nap1•Kap114•H2A-H2B, and further classified using Heterogenous Refinement. 54,170 particles of Nap1•H2A-H2B•Kap114 and 59,310 particles of Nap1•Kap114•H2A-H2B were further refined using Non-Uniform (NU) Refinement resulting in 4.02 Å and 3.65 Å maps, respectively. To obtain more particles, these maps were used to generated templates for additional template picking on cryoSPARC. This resulted in 4,314,112 total particles that contained Nap1 only, Kap114•H2A-H2B, Nap1•H2A-H2B•Kap114 and Nap1•Kap114•H2A-H2B. After the first round of 2D classification ~1 million particles were further processed for Nap1 core dimer, and another ~1 million particles were further processed for the Kap114-containing complexes. Both Nap1 and Kap114 complexes underwent three more rounds of additional 2D classifications to obtain 468,627 and 675,417 particles, respectively. Two Ab-initio classes were generated for Nap1 particles, and four Ab-initio classes were generated for the Kap114 complexes followed by classification by Heterogeneous Refinement. 230,210 Nap1 particles were used in NU Refinement resulting in the final map with 3.2 Å resolution. The Nap1•H2A-H2B•Kap114 and Nap1•Kap114•H2A-H2B particles obtained from Topaz were merged with ones obtained from template picking. Duplicates were then removed, resulting in 136,011 Nap1•H2A-H2B•Kap114 and 148,410 Nap1•Kap114•H2A-H2B final particles that were used for reconstruction in NU Refinement to obtain maps with 3.5 and 3.2 Å, respectively.

The cryo-EM initial model for Nap1 was generated with AlphaFold-Multimer (39). The Nap1•Kap114•H2A-H2B complex used 8F0X, Alpha-Fold model of Kap114 from UniProt (AF-P53067-F1), and the cryo-EM model of Nap1, while the Nap1•H2A-H2B•Kap114 complex used 8F1E, AF-P53067-F1, and the cryo-EM model of Nap1. All

the models were roughly docked into the map using UCSF Chimera (40) and then subjected to real-space refinement with global minimization and rigid body restraints in Phenix (41). The resulting models were then manually rebuilt and refined using Coot (42), further corrected using ISOLDE (43) on UCSF ChimeraX (44) and subjected to last round of refinement in Phenix. We used PDBe PISA to calculate surface area accessibility (45). We also used PyMOL version 2.5 and the APBS electrostatic plugin for 3D structure and electrostatic analysis (46, 47).

**SAXS methods**

To form the Nap1•Kap114 complex, a molar ratio of 1:3 Nap1 dimer:Kap114 were mixed before purification using the Superdex200 Increase 10/300 column and the following buffer: 20 mM HEPES pH 7.4, 150 mM NaCl, 5% glycerol, and 1 mM TCEP. The protein complex, concentrated to 3 mg/mL, and the size exclusion chromatography buffer were both flash frozen to ensure precise buffer match. Measurements were taken with sample concentration between 1 – 3mg/mL at 10°C using the SAXS instrument at the 12-ID-B beamline of the Advanced Photon Source, Argonne National Laboratory. To eliminate all possible aggregates, samples were centrifuged at 15,000xg for 30 min, and only the top 50% of the solution was used for data measurement. To prevent potential radiation damage, samples were measured in a quartz capillary flow cell with a diameter of 1.5 mm under a constant flow rate of 10 µL/s. Each sample measurement was purged with its matching buffer solution. Data were collected using the Pilatus 2M area detector with a beam energy of 14k eV and beam current of 500 mA. 40 successive frames with an exposure of 1 s were recorded for each sample and the data was averaged for better

signal/noise statistics. Scattering profiles were averaged, reduced, and merged from measurements at different concentrations using BioXTAS RAW software (48). Structural parameters and the distance distribution function, *P*(*r*), were calculated with GNOM (49) and the ab initio electron density was reconstructed using DENSS (50).

**Acknowledgments**

We thank all members of the Structural Biology Laboratory (SBL) and the CEMF in UTSW for their expert assistance with cryo-EM data collection. We greatly appreciate Macromolecular Biophysics Resource (MBR) and Chad Brautigam for discussion and use of the AUC and Mass Photometer. We also thank the Erzberger lab for using their plate reader for FP assays. SBL and CEMF at UTSW are partially supported by grant RP170644 from the Cancer Prevention & Research Institute of Texas (CPRIT). The Refeyn Mass Photometer in MBR was supported by grant S10-OD030312 from the National Institute of Health. We thank the D'Arcy lab for the use of their SEC-MALS equipment and Joy Shaffer for training. Molecular graphics and analyses performed with UCSF ChimeraX, developed by the Resource for Biocomputing, Visualization, and Informatics at the University of California, San Francisco, with support from National Institutes of Health R01-GM129325 and the Office of Cyber Infrastructure and Computational Biology, National Institute of Allergy and Infectious Diseases. This research used resources of the Advanced Photon Source, a U.S. Department of Energy (DOE) Office of Science user facility operated for the DOE Office of Science by Argonne National Laboratory under Contract No. DE-AC02-06CH11357. This work was funded by NIGMS of NIH under Awards R35GM141461 (Y.M.C.), R01GM069909 (Y.M.C.),

T32GM008203 (J.J), the Welch Foundation Grants I-1532 (Y.M.C.), support from the Alfred and Mabel Gilman Chair in Molecular Pharmacology, Eugene McDermott Scholar in Biomedical Research (Y.M.C.) and the Gilman Special Opportunities Award (H.Y.J.F.).

**References**

1. E. I. Campos *et al.*, The program for processing newly synthesized histones H3.1 and H4. *Nat Struct Mol Biol* **17**, 1343-1351 (2010).

2. H. Tagami, D. Ray-Gallet, G. Almouzni, Y. Nakatani, Histone H3.1 and H3.3 complexes mediate nucleosome assembly pathways dependent or independent of DNA synthesis. *Cell* **116**, 51-61 (2004).

3. L. J. Benson *et al.*, Modifications of H3 and H4 during chromatin replication, nucleosome assembly, and histone exchange. *J Biol Chem* **281**, 9287-9296 (2006).

4. M. Baake, D. Doenecke, W. Albig, Characterisation of nuclear localisation signals of the four human core histones. *J Cell Biochem* **81**, 333-346 (2001).

5. P. Muhlhausser, E. C. Muller, A. Otto, U. Kutay, Multiple pathways contribute to nuclear import of core histones. *EMBO Rep* **2**, 690-696 (2001).

6. K. Schwamborn, W. Albig, D. Doenecke, The histone H1(0) contains multiple sequence elements for nuclear targeting. *Exp Cell Res* **244**, 206-217 (1998).

7. N. E. Bernardes, Y. M. Chook, Nuclear import of histones. *Biochem Soc Trans* **48**, 2753-2767 (2020).

8. M. Seidel *et al.*, Co-translational binding of importins to nascent proteins. *bioRxiv* 10.1101/2022.11.02.514836, 2022.2011.2002.514836 (2022).

9. N. Mosammaparast, C. S. Ewart, L. F. Pemberton, A role for nucleosome assembly protein 1 in the nuclear transport of histones H2A and H2B. *EMBO J* **21**, 6527-6538 (2002).

10. L. Chang *et al.*, Histones in transit: cytosolic histone complexes and diacetylation of H4 during nucleosome assembly in human cells. *Biochemistry* **36**, 469-480 (1997).

11. X. Chen *et al.*, Histone Chaperone Nap1 Is a Major Regulator of Histone H2A-H2B Dynamics at the Inducible GAL Locus. *Mol Cell Biol* **36**, 1287-1296 (2016).

12. Y. Huang, Y. Dai, Z. Zhou, Mechanistic and structural insights into histone H2A-H2B chaperone in chromatin regulation. *Biochem J* **477**, 3367-3386 (2020).

13. C. M. Hammond, C. B. Stromme, H. Huang, D. J. Patel, A. Groth, Histone chaperone networks shaping chromatin function. *Nat Rev Mol Cell Biol* **18**, 141-158 (2017).

14. N. Mosammaparast *et al.*, Nuclear import of histone H2A and H2B is mediated by a network of karyopherins. *J Cell Biol* **153**, 251-262 (2001).

15. N. Mosammaparast, B. C. Del Rosario, L. F. Pemberton, Modulation of histone deposition by the karyopherin kap114. *Mol Cell Biol* **25**, 1764-1778 (2005).

16. K. Luger, A. W. Mader, R. K. Richmond, D. F. Sargent, T. J. Richmond, Crystal structure of the nucleosome core particle at 2.8 A resolution. *Nature* **389**, 251-260 (1997).

17. C. Aguilar-Gurrieri *et al.*, Structural evidence for Nap1-dependent H2A-H2B deposition and nucleosome assembly. *EMBO J* **35**, 1465-1482 (2016).

18. Y. J. Park, S. J. McBryant, K. Luger, A beta-hairpin comprising the nuclear localization sequence sustains the self-associated states of nucleosome assembly protein 1. *J Mol Biol* **375**, 1076-1085 (2008).

19. C. C. Liao *et al.*, Karyopherin Kap114p-mediated trans-repression controls ribosomal gene expression under saline stress. *EMBO Rep* **21**, e48324 (2020).

20. J. Jiou *et al.*, Mechanism of RanGTP priming H2A-H2B release from Kap114 in an atypical RanGTP•Kap114•H2A-H2B complex. *bioRxiv* 10.1101/2022.11.22.517512, 2022.2011.2022.517512 (2023).

21. P. Sarkar, N. Akhavantabib, S. D'Arcy, Comprehensive analysis of histone-binding proteins with multi-angle light scattering. *Methods* **184**, 93-101 (2020).

22. P. Sarkar, N. Zhang, S. Bhattacharyya, K. Salvador, S. D'Arcy, Characterization of Caenorhabditis elegans Nucleosome Assembly Protein 1 Uncovers the Role of Acidic Tails in Histone Binding. *Biochemistry* **58**, 108-113 (2019).

23. A. Bowman *et al.*, The histone chaperones Nap1 and Vps75 bind histones H3 and H4 in a tetrameric conformation. *Mol Cell* **41**, 398-408 (2011).

24. M. Noda *et al.*, Assembly states of the nucleosome assembly protein 1 (NAP-1) revealed by sedimentation velocity and non-denaturing MS. *Biochem J* **436**, 101-112 (2011).

25. J. L. Hodges *et al.*, Nuclear import of TFIIB is mediated by Kap114p, a karyopherin with multiple cargo-binding domains. *Mol Biol Cell* **16**, 3200-3210 (2005).

26. A. Padavannil *et al.*, Importin-9 wraps around the H2A-H2B core to act as nuclear importer and histone chaperone. *Elife* **8** (2019).

27. A. Bowman *et al.*, The histone chaperones Vps75 and Nap1 form ring-like, tetrameric structures in solution. *Nucleic Acids Res* **42**, 6038-6051 (2014).

28. J. Jiou *et al.*, Mechanism of RanGTP priming the release of H2A-H2B from Kap114 and Importin-9. *bioRxiv* 10.1101/2022.11.22.517512, 2022.2011.2022.517512 (2022).

29. H. Zhao *et al.*, Recorded scan times can limit the accuracy of sedimentation coefficients in analytical ultracentrifugation. *Anal Biochem* **437**, 104-108 (2013).

30. T. M. S. Laue, B.; Ridgeway, T.M.; Pelletier, S.L. , "Computer-aided Interpretation of Sedimentation Data for Proteins" in Analytical Ultracentrifugation in Biochemistry and Polymer Science. (Royal Society of Chemistry, Cambridge, U.K. , 1992), pp. 90-125.

31. P. Schuck, Size-distribution analysis of macromolecules by sedimentation velocity ultracentrifugation and lamm equation modeling. *Biophys J* **78**, 1606-1619 (2000).

32. C. A. Brautigam, Calculations and Publication-Quality Illustrations for Analytical Ultracentrifugation Data. *Methods Enzymol* **562**, 109-133 (2015).

33. H. Zhao, G. Piszczek, P. Schuck, SEDPHAT--a platform for global ITC analysis and global multi-method analysis of molecular interactions. *Methods* **76**, 137-148 (2015).

34. H. Y. J. Fung, Y. M. Chook, Binding Affinity Measurement of Nuclear Export Signal Peptides to Their Exporter CRM1. *Methods Mol Biol* **2502**, 245-256 (2022).

35. T. H. Scheuermann, S. B. Padrick, K. H. Gardner, C. A. Brautigam, On the acquisition and analysis of microscale thermophoresis data. *Anal Biochem* **496**, 79-93 (2016).

36. D. N. Mastronarde, Automated electron microscope tomography using robust prediction of specimen movements. *J Struct Biol* **152**, 36-51 (2005).

37. A. Punjani, J. L. Rubinstein, D. J. Fleet, M. A. Brubaker, cryoSPARC: algorithms for rapid unsupervised cryo-EM structure determination. *Nat Methods* **14**, 290-+ (2017).

38. T. Bepler *et al.*, Positive-unlabeled convolutional neural networks for particle picking in cryo-electron micrographs. *Nat Methods* **16**, 1153-1160 (2019).

39. R. Evans *et al.*, Protein complex prediction with AlphaFold-Multimer. *bioRxiv* 10.1101/2021.10.04.463034, 2021.2010.2004.463034 (2022).

40. E. F. Pettersen *et al.*, UCSF chimera - A visualization system for exploratory research and analysis. *J Comput Chem* **25**, 1605-1612 (2004).

41. P. D. Adams *et al.*, PHENIX: a comprehensive Python-based system for macromolecular structure solution. *Acta Crystallogr D* **66**, 213-221 (2010).

42. P. Emsley, New Tools for Ligand Refinement and Validation in Coot and CCP4. *Acta Crystallogr A* **74**, A390-A390 (2018).

43. T. I. Croll, ISOLDE: a physically realistic environment for model building into low-resolution electron-density maps. *Acta Crystallogr D Struct Biol* **74**, 519-530 (2018).

44. E. F. Pettersen *et al.*, UCSF ChimeraX: Structure visualization for researchers, educators, and developers. *Protein Sci* **30**, 70-82 (2021).

45. E. Krissinel, K. Henrick, Inference of macromolecular assemblies from crystalline state. *J Mol Biol* **372**, 774-797 (2007).

46. Schrodinger, LLC (2020) The PyMOL Molecular Graphics System, Version 2.4.

47. E. Jurrus *et al.*, Improvements to the APBS biomolecular solvation software suite. *Protein Sci* **27**, 112-128 (2018).

48. J. B. Hopkins, R. E. Gillilan, S. Skou, BioXTAS RAW: improvements to a free open-source program for small-angle X-ray scattering data reduction and analysis. *J Appl Crystallogr* **50**, 1545-1553 (2017).

49. A. V. Semenyuk, D. I. Svergun, GNOM– a program package for small-angle scattering data processing. *Journal of Applied Crystallography* **24**, 537-540 (1991).

50. T. D. Grant, Ab initio electron density determination directly from solution scattering data. *Nat Methods* **15**, 191-193 (2018).

**Table 1. Cryo-EM data collection, refinement, and validation statistics**

| | Nap1 core | Nap1·Kap114 ·H2A-H2B | Nap1·H2A-H2B ·Kap114 |
|---|---|---|---|
| **Data collection and processing** | | | |
| Magnification | 105,000X | | |
| Voltage (kV) | 300 | | |
| Electron exposure ($e^{-}$/Å$^2$) | 52 | | |
| Defocus range (μm) | 1.5-2.5 | | |
| Pixel size (Å) | 0.415 | | |
| Symmetry imposed | C1 | | |
| Initial particle images (no.) | 4,314,112 | | |
| Final particle images (no.) | 230,210 | 148,410 | 113,011 |
| Map resolution (Å) | 3.21 | 3.20 | 3.54 |
| FSC threshold | 0.143 | 0.143 | 0.143 |
| **Refinement** | | | |
| Initial model used (PDB code) | AlphaFold-multimer Nap1 FL | AF-P53067-F1, 8F0X, cryoEM Nap1 | AF-P53067-F1, 8F1E, cryoEM Nap1 |
| Model resolution (Å) | 3.0/3.2/4.3 | 3.1/3.1/3.4 | 3.4/3.5/3.9 |
| FSC threshold | 0/0.143/0.5 | 0/0.143/0.5 | 0/0.143/0.5 |
| Map sharpening *B* factor (Å$^2$) | 158.4 | 126.5 | 165.0 |
| Model composition | | | |
| Non-hydrogen Atoms | 4,670 | 13,529 | 13,408 |
| Protein residues | 568 | 1,682 | 1,668 |
| *B* factors (Å$^2$) | 196.99 | 129.6 | 317.38 |
| R.m.s. deviations | | | |
| Bond lengths (Å) | 0.003 | 0.004 | 0.002 |
| Bond angles (°) | 0.592 | 0.543 | 0.505 |
| CCvolume/mask | 0.68/0.69 | 0.76/0.76 | 0.74/0.74 |
| **Validation** | | | |
| MolProbity score | 1.69 | 1.30 | 1.46 |
| Clashscore | 10.54 | 5.54 | 7.64 |
| Poor rotamers (%) | 0 | 0 | 0 |
| Ramachandran plot | | | |
| Favored (%) | 97.16 | 98.26 | 97.82 |
| Allowed (%) | 2.84 | 1.74 | 2.18 |
| Disallowed (%) | 0 | 0 | 0 |
| CaBLAM outliers (%) | 1.25 | 1.15 | 1.04 |
| EMRinger score | 0.94 | 1.93 | 1.06 |
| **EMD/PDB ID** | | | |